Role of sphingolipid metabolism signaling in a novel mouse model of renal osteodystrophy based on transcriptomic approach

Yujia Wang[1,2], Yan Di[1,2], Yongqi Li[1,2], Jing Lu[1,2], Bofan Ji[1,2], Yuxia Zhang[1,2], Zhiqing Chen[1,2], Sijie Chen[1,2], Bicheng Liu[1], Rining Tang[2]

[1]Institute of Nephrology, Zhong Da Hospital, Southeast University School of Medicine, Nanjing, Jiangsu 210003, China;
[2]Institute of Nephrology, NanJing LiShui People's Hospital, Zhongda Hospital Lishui Branch, Southeast University School of Medicine, Nanjing, Jiangsu 211200, China.

Abstract

Background: Renal osteodystrophy (ROD) is a skeletal pathology associated with chronic kidney disease-mineral and bone disorder (CKD-MBD) that is characterized by aberrant bone mineralization and remodeling. ROD increases the risk of fracture and mortality in CKD patients. The underlying mechanisms of ROD remain elusive, partially due to the absence of an appropriate animal model. To address this gap, we established a stable mouse model of ROD using an optimized adenine-enriched diet and conducted exploratory analyses through ribonucleic acid sequencing (RNA-seq).

Methods: Male 8-week-old C57BL/6J mice were randomly allocated into three groups: control group (n = 5), adenine and high-phosphate (HP) diet group (n = 20), and the optimized adenine-containing diet group (n = 20) for 12 weeks. We assessed the skeletal characteristics of model mice through blood biochemistry, microcomputed tomography (micro-CT), and bone histomorphometry. RNA-seq was utilized to profile gene expression changes of ROD. We elucidated the functions of differentially expressed genes (DEGs) using gene ontology (GO) analysis, Kyoto Encyclopedia of Genes and Genomes (KEGG) pathway analysis, and gene set enrichment analysis (GSEA). DEGs were validated via quantitative real-time polymerase chain reaction (qRT-PCR).

Results: By the fifth week, adenine followed by an HP diet induced rapid weight loss and high mortality rates in the mouse group, precluding further model development. Mice with optimized adenine diet-induced ROD displayed significant abnormalities in serum creatinine and blood urea nitrogen levels, accompanied by pronounced hyperparathyroidism and hyperphosphatemia. The femur bone mineral density (BMD) of the model mice was lower than that of control mice, with substantial bone loss and cortical porosity. ROD mice exhibited substantial bone turnover with an increase in osteoblast and osteoclast markers. Transcriptomic profiling revealed 1907 genes with upregulated expression and 723 genes with downregulated expression in the femurs of ROD mice relative to those of control mice. Pathway analyses indicated significant enrichment of upregulated genes in the sphingolipid metabolism pathway. The significant upregulation of alkaline ceramidase 1 (*Acer1*), alkaline ceramidase 2 (*Acer2*), prosaposin-like 1 (*Psapl1*), adenosine A1 receptor (*Adora1*), and sphingosine-1-phosphate receptor 5 (*S1pr5*) were successfully validated in mouse femurs by qRT-PCR.

Conclusions: Optimized adenine diet mouse model may be a valuable proxy for studying ROD. RNA-seq analysis revealed that the sphingolipid metabolism pathway is likely a key player in ROD pathogenesis, thereby providing new avenues for therapeutic intervention.

Keywords: Chronic kidney disease-mineral and bone disorder; Renal osteodystrophy; Adenine; Phosphate; Transcriptomics; Sphingolipids

Introduction

Chronic kidney disease-mineral and bone disorder (CKD-MBD) is a prevalent complication in patients with CKD.[1] As the skeletal manifestation of CKD-MBD, renal osteodystrophy (ROD) has emerged as a significant global health concern. Due to the lack of a stable animal model and incomplete understanding of its mechanisms, therapeutic approaches for ROD have demonstrated limited efficacy.[2] Consequently, there is an exigent need for a suitable animal model to elucidate ROD mechanisms and develop more effective treatments.

Recently, numerous methods have been employed to establish models of ROD, including specialized diets,[3–16] surgical techniques,[17–22] chemical drug induction,[23,24] and transgenic animal models harboring spontaneous CKD.[25–29] The characteristics of these ROD animal models are summarized in Supplementary Material 1, http://links.lww.com/CM9/C115. Nevertheless, these models are limited in use due to several shortcomings. There is inconsistency and a lack of transparency in the specialized diets used across different experiments, with variations also seen in the duration of specialized diet induction. Surgical

Access this article online

Quick Response Code:

Website: www.cmj.org

DOI: 10.1097/CM9.0000000000003261

Correspondence to: Rining Tang, Institute of Nephrology, NanJing LiShui People's Hospital, Zhongda Hospital Lishui Branch, Southeast University, Nanjing, Jiangsu 211200, China
E-Mail: tangrn77@163.com

Chinese Medical Journal 2024;XX(XX)
Received: 14-12-2023; **Online:** 16-08-2024 **Edited by:** Yuanyuan Ji

methods demand surgical expertise and postoperative care, complicating the assurance of consistent effects. Additionally, the nephrectomy model has an exceedingly high morbidity rate, and the sudden renal failure it causes does not reflect the chronic pathophysiology of CKD.[30] Chemical drug induction can result in severe liver injury. Transgenic animal models fail to closely mimic the mineral disorder of ROD, and moreover, these studies on the ROD model did not provide specific data on survival rates or success rates over the study period. Hence, the applicability of the aforementioned models should be evaluated critically.

In a preliminary study by our group, we applied adenine and a high-phosphate (HP) diet in rats for 34 weeks to evaluate skeletal abnormalities.[12] However, our previous study had certain limitations. The extended duration of the study made excluding confounding factors challeging. Furthermore, employing an HP diet to simulate secondary hyperparathyroidism (SHPT) oversimplifies the complexity of ROD. Notably, mice may be more practical and manageable for subsequent in-depth experiments, such as gene editing and modification. Considering these factors, we developed a stable and precise mouse model to explore the potential mechanisms involved in ROD.

ROD is a multifaceted and challenging bone disorder, wherein the cellular and molecular alterations within bone tissues play a critical role.[31] Currently, RNA sequencing (RNA-seq) and transcriptomic analysis have emerged as pioneering techniques that have allowed researchers to discover novel molecular metabolisms of ROD.[32]

In this study, we developed a more stable and reliable mouse model of ROD utilizing an optimized adenine diet. By employing transcriptomic analysis, we identified alterations in sphingolipid metabolism pathways and several significant molecular targets. Our comprehensive study has the potential to yield novel insights into the pathogenesis of ROD.

Methods

Animals and experimental design

Male C57Bl/6J mice, aged 6 weeks and weighing 18 ± 2 g, were acquired from Vital River Laboratories (Zhejiang, China) under license No. SCXK (Zhe) 2021-0006. They were maintained in a specific pathogen-free facility, allocated five per cage, with a consistent 12:12-h light/dark cycle, at a temperature of 23°C ± 2°C and a relative humidity of 50 ± 10%. Access to purified water and rodent chow was provided *ad libitum*. All animal experimental procedures were approved by the Institutional Animal Care and Use Committee of Southeast University (No. 20210228021).

Following a two-week period of acclimation and weight gain, the mice were randomly allocated into three groups: (1) control (CTL) group ($n = 5$), (2) adenine and HP diet group ($n = 20$), and (3) the optimized adenine-containing diet group ($n = 20$). The adenine and HP diet group underwent a four-week intervention with an adenine-enriched diet (0.2% adenine based on AIN-93G purified feed; Jiangsu Xietong Pharmaceutical Bioengineering Co., Ltd., Nanjing, China), followed by an HP regimen (1.8% phosphate, devoid of supplemental adenine, based on AIN-93G purified feed; Jiangsu Xietong Pharmaceutical Bioengineering Co., Ltd.). Concurrently, the optimized adenine-containing diet group was administered a diet comprising 0.2% adenine (A8626, Sigma-Aldrich, Saint Louis, USA), 1% calcium, 1% phosphate, and 19% protein, adhering to the AIN-93G purified feed composition (Jiangsu Xietong Pharmaceutical Bioengineering Co., Ltd.) for the entire 12-week duration of the study. The CTL group received standard rodent chow without any supplemental adenine or phosphate (AIN-93G purified feed, Jiangsu Xietong Pharmaceutical Bioengineering Co., Ltd.). The specific formulations of the feed are provided in Supplementary Material 2, http://links.lww.com/CM9/C115.

Throughout the experimental period, the body weight of the mice was recorded on a weekly basis. At the conclusion of the twelfth week, all mice were euthanized, and blood samples were extracted and subjected to centrifugation at 3000 × *g* for 15 min. The resulting serum was then preserved at −80°C for subsequent analysis using commercial assay kits and enzyme-linked immunosorbent assays (ELISAs). Additionally, the kidneys and both hind limbs, including the femurs and tibias, were collected and preserved for histopathological evaluation and immunohistochemistry (IHC) staining.

Biochemical analysis

Serum creatinine (Cr), blood urea nitrogen (BUN), calcium (Ca), and phosphate (P) concentrations were quantified using an automatic biochemical analyzer (Chemray 800, Shenzhen Mindray Bio-Medical Electronics Co., Ltd. Shenzhen, China). For these measurements, commercial assay kits were used (Cat No.: S03076 and S03036 for Cr and BUN, respectively; Shenzhen Mindray; and Cat No.: C057 and C014 for Ca and P, respectively; Changchun Huili Biotech Co., Ltd. Changchun, China) according to the manufacturer's instructions.

Blood samples for cellular analysis were collected in lithium heparin-coated tubes (BD 367884; Becton Dickinson, Franklin Lakes, NJ, USA). Hemoglobin levels and red blood cell counts were determined using an automated veterinary hematology analyzer (Mindray BC-2800vet, Shenzhen, China).

ELISA

Serum parathyroid hormone (PTH) concentrations were measured using ELISA kits (Cat No. E-El-M0709c, Elabscience, Wuhan, China). All assays were conducted in strict accordance with the manufacturer's protocols.

Histopathological assessments

Kidney and femur samples from mice were fixed in 4% phosphate-buffered paraformaldehyde (Bl539a, Bio-sharp,

Guangzhou, China) for 24 h and subsequently embedded in paraffin. Serial sections of 4 μm thickness were prepared and stained using hematoxylin and eosin (HE), periodic acid-Schiff (PAS), and masson trichrome (G1005, G1008, G1006 Servicebio, Wuhan, China) according to the manufacturer's instructions.

For bone histopathological analysis, the right femurs were extracted and meticulously denuded of soft tissue using a scalpel. These femur samples were fixed in 4% paraformaldehyde and subsequently decalcified using an ethylene diamine tetraacetic acid (EDTA)-based solution (Servicebio Biological Co., Ltd., Wuhan, China) over a three-week period. The specimens underwent dehydration and defatting processes before being sectioned at a thickness of 4 μm using a Leica RM2016 microtome (Leica Microsystems, Shanghai, China). Staining with tartrate-resistant acid phosphatase (TRAP) (G1050, Servicebio) was executed in accordance with the instructions.

Images were acquired using a DM 3000 light microscope (Leica Microsystems, Deerfield, IL, USA). The slides were subjected to semi-quantitative assessment by a single investigator who was blinded to the allocation of treatment groups.

Microcomputed tomography (micro-CT) scanning and image reconstruction

The fixed right femur samples were preserved in 4% paraformaldehyde and imaged using a micro-CT SkyScan 1176 system (Bruker Analytical Instruments, Kontich, Belgium). The analysis of bone microarchitecture at the metaphysis region of the distal femur focused on a specific set of parameters: bone mineral density (BMD), total tissue volume (TV), bone volume (BV), bone volume ratio (BV/TV), bone surface area (BS), bone surface density (BS/TV), trabecular number (Tb.N), trabecular thickness (Tb.Th), and trabecular separation (Tb.Sp). Additionally, the cortical bone geometry, including area and thickness, was quantified at the femoral midshaft. The metaphyseal scanning region of the intact femur included 150 slices, starting 1 mm proximal to the growth plate and extending distally. For the diaphyseal region, which is situated midway between the femoral head and distal condyles, the scanning included 100 slices centered on the midshaft. All animals were scanned at a resolution of 18 μm. The data were processed using Skyscan CT Analyzer software (CTAn, Bruker, Germany). Two-dimensional (2D) images were rendered with DataViewer (SkyScan software), and three-dimensional (3D) reconstructions and animations were generated using CTvox (SkyScan software).

IHC analysis of femurs

The femur sections were deparaffinized and subjected to antigen retrieval using pepsin solution (Servicebio Biological Co., Ltd.). Subsequently, they were blocked with bovine serum albumin (HyClone, Logan, UT, USA) or 30 min before overnight incubation at 4°C with the following primary antibodies: anti-Osterix (GB111900, 1:100 dilution, Servicebio Biological Co., Ltd.) and anti-cathepsin K (GB111276, 1:200 dilution, Servicebio Biological Co., Ltd.). Following three washes the next day, the sections were incubated with horseradish peroxidase (HRP)-conjugated goat anti-rabbit IgG for 50 min at room temperature. 3, 3′-diaminobenzidine (DAB) stain (Servicebio Biological Co., Ltd.) was then applied, and tap water was used to terminate the reaction. Nuclei were counterstained using hematoxylin (Servicebio Biological Co., Ltd.) for 3 min. Imaging was performed with a DM 3000 light microscope (Leica Microsystems), and image analysis was conducted using Image-Pro Plus 6.0 software (Media Cybernetics, Inc., Rockville, MD, USA).

RNA isolation and library preparation

Total RNA was extracted using Trizol reagent (Invitrogen, CA, USA) according to the manufacturer's instructions. The purity and concentration of the extracted RNA were assessed with a NanoDrop 2000 spectrophotometer (Thermo Scientific, Waltham, MA, USA), while RNA integrity was verified using an Agilent 2100 Bioanalyzer (Agilent Technologies, Santa Clara, CA, USA). Subsequently, sequencing libraries were prepared utilizing the VAHTS Universal V6 RNA-seq Library Prep Kit (Vazyme Biotech Co., Ltd., Nanjing, China) according to the manufacturer's protocol. Transcriptome sequencing and subsequent bioinformatic analysis were conducted by OE Biotech Co., Ltd. (Shanghai, China).

RNA-seq and differentially expressed genes (DEGs) analysis

Sequencing of the libraries was performed on an Illumina NovaSeq 6000 platform (San Diego, CA, USA), generating approximately 150 bp paired-end reads, with approximately 51 million raw reads produced per sample. The raw fastq format reads were first processed using Fastq,[33] during which low-quality reads were removed to procure high-quality, clean reads. Approximately 48 million clean reads per sample were retained for further analysis. These reads were mapped to the reference genome utilizing hierarchical graph fm index for sequence alignment (HISAT2) (http://ccb.jhu.edu/software/hisat2).[34] Gene expression levels were quantified as fragments per kilobase million (FPKM),[35] and read counts were derived using HTSeq-count (https://htseq.readthedocs.io/en/latest/tour.html).[36] Principal component analysis (PCA) was performed in R (version 3.2.0, https://www.r-project.org/) to assess the replicability of the biological samples. Differential expression analysis was performed using DESeq2 (https://github.com/mikelove/DESeq2),[37] with a q-value of <0.05 and a fold change >2 or <0.5 set as the thresholds for identifying significant DEGs. Hierarchical clustering analysis of DEGs was also performed in R (version 3.2.0) to visualize the expression patterns across different groups and samples. The top 30 genes were represented on a radar chart, which was generated using the R package "grader," to display the expression of DEGs with upregulated or downregulated expression. Both Gene Ontology (GO)[38] and Kyoto Encyclopedia of Genes and Genomes (KEGG)[39] pathway enrichment analyses of DEGs were conducted based on the hypergeometric distribution to identify significantly enriched terms, again employing R (version 3.2.0) for visualization purposes. This process involved the creation

of column, chord, and bubble diagrams to represent the significantly enriched terms. Finally, gene set enrichment analysis (GSEA) was implemented using GSEA software (http://software.broadinstitute.org/gsea/index.jsp).[40,41] This analysis utilized a predefined gene set, ranking the genes by their differential expression between two sample types and testing for enrichment at the extremes of the ranked list.

Quantitative real-time polymerase chain reaction (qRT-PCR)

RNA was extracted from the femur and tibia tissues of different groups of mice using Trizol reagent (R401-01, Vazyme, China). The integrity and quality of the extracted RNA were assessed using a NanoDrop 2000 spectrophotometer (Thermo Scientific). The RNA was subsequently reverse-transcribed to complementary deoxyribo nucleic acid (cDNA) using HIScript III RT Super Mix (R323-01, Vazyme, China). Quantitative polymerase chain reaction (qPCR) amplification was performed using ChamQ SYBR qPCR Master Mix (R341-02, Vazyme). The sequences of primers used for qRT-PCR are listed in Supplementary Material 3, http://links.lww.com/CM9/C115. Relative messenger ribonucleic acid (mRNA) expression was normalized to that of glyceraldehyde 3-phosphate dehydrogenase (GAPDH) and calculated using the $2^{-\Delta\Delta\text{cycle threshold (Ct)}}$ method.

Statistical analysis

All results were presented as mean ± standard error of the mean (SEM). The number of experimental mice was ≥5 per group, except for the adenine and an HP diet group, which had four remaining mice. Differences among multiple groups were analyzed using one-way analysis of variance (ANOVA) followed by the Bonferroni *post hoc* correction. Differences between two groups were evaluated using an unpaired Student's *t*-test. Variances between the groups were compared using the *F*-test; if variances were unequal, an unpaired *t*-test with Welch's correction was applied. All statistical analyses were conducted using Prism 9.0 (GraphPad Prism Software, USA). A *P*-value of <0.05 was considered statistically significant.

Results

Survival rate and body weight of model mice with optimized adenine diet-induced ROD

Our previous studies showed that rats with CKD develop bone abnormalities when subjected to a regimen consisting of four weeks of a 0.2% adenine diet followed by 30 weeks of an HP diet (1.8% phosphate without additional adenine). To induce ROD, 20 mice ($n = 20$) were initially fed a diet supplemented with 0.2% adenine (incorporated into the AIN-93G base diet) for four weeks, followed by a 1.8% HP diet upon the cessation of dietary adenine. Concurrently, we devised an optimized adenine diet by adding 0.2% adenine, 1% phosphate, 1% calcium, and 1 IU/g vitamin D to the AIN-93G base diet. This optimized diet was administered to a separate group of 20 mice ($n = 20$) for the duration of the study, as depicted in Figure 1A.

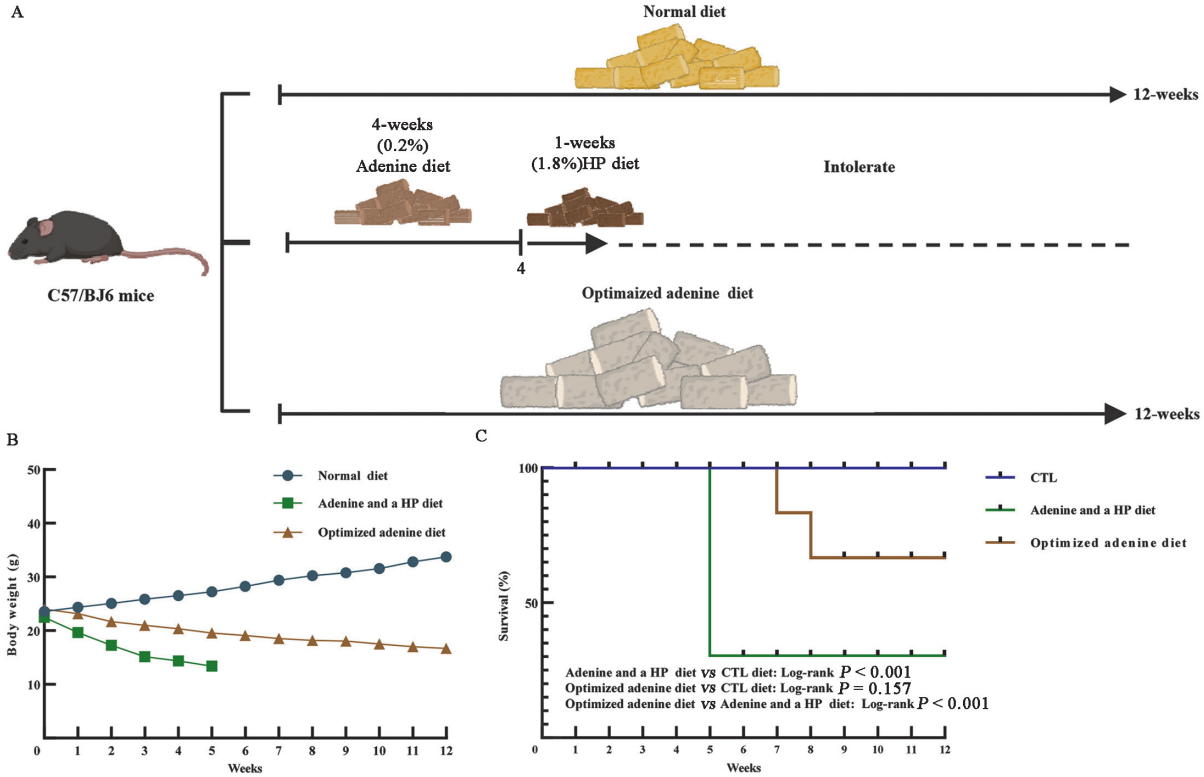

Figure 1: Experimental protocol, body weight, and survival rate of the three groups. (A) Experimental protocol for establishing the three groups. (B) Curves of body weight changes in the different groups. (C) Survival rates in mice of three groups. Data are presented as mean ± SEM. $n = 5$ for the CTL group with a standard diet, $n = 20$ for the adenine and high phosphate diet group (at week 5, only four mice survived), $n = 20$ for the optimized adenine diet group (only two deaths occurring at the seventh week and the eighth week). HP: High-phosphate; SEM: Standard error of the mean.

Unexpectedly, in the group receiving adenine followed by an HP diet, a marked decrease in body weight was observed starting from the second week of induction. This weight decline was so severe that 80% of the mice perished the second week of the HP diet. The final surviving four mice had an average body weight of 13.38 g. In contrast, the mice that consumed the optimized adenine diet exhibited a significantly slower reduction in weight, as illustrated in Figure 1B. This dietary modification markedly increased survival rates, with only two deaths among the mice on the optimized diet [Figure 1C] (Adenine and an HP diet *vs*. CTL diet: log-rank P <0.001; optimized adenine diet *vs*. CTL diet: log-rank P = 0.16; optimized adenine diet *vs*. adenine and an HP diet: log-rank P <0.001).

Renal impairment and biochemical abnormalities in model mice with optimized adenine diet-induced ROD

The renal function of ROD model mice was evaluated by quantifying the serum creatinine and BUN levels. Compared with those in the control group, the optimized adenine diet group exhibited markedly elevated levels of serum creatinine and BUN. Mice survived in adenine and an HP diet group displayed significantly more pronounced renal dysfunction compared to those on the optimized adenine diet [Figure 2A, one-way ANOVA, F = 30.79, P <0.001; Figure 2B, one-way ANOVA, F = 55.69, P <0.001]. HE staining and PAS staining of kidney sections demonstrated characteristic features of CKD induced by the optimized adenine diet, such as dilation of proximal and distal tubules, epithelial flattening, loss of the proximal brush border, basement membrane thickening, and tubulointerstitial cellular infiltration [Figure 2C, D]. Furthermore, Masson's trichrome staining highlighted renal interstitial fibrosis in the CKD model precipitated by the optimized adenine diet [Figure 2E]. Collectively, these findings confirmed kidney injury in our optimized adenine diet-induced CKD model.

According to the CKD-MBD guidelines,[1] CKD-MBD is characterized by elevated serum Pi and PTH levels. Model mice on optimized adenine diet exhibited significantly greater serum phosphorus concentrations [Figure 2F, unpaired t-test with Welch's correction, t = 9.29, P <0.001]. Concurrent with the changes in the serum phosphorus level, the PTH level also substantially increased in the mice fed the optimized adenine diet [Figure 2H, unpaired t-test, t = 5.46, P <0.001]. However, there was no significant difference in serum calcium levels between the two groups [Figure 2G]. These findings

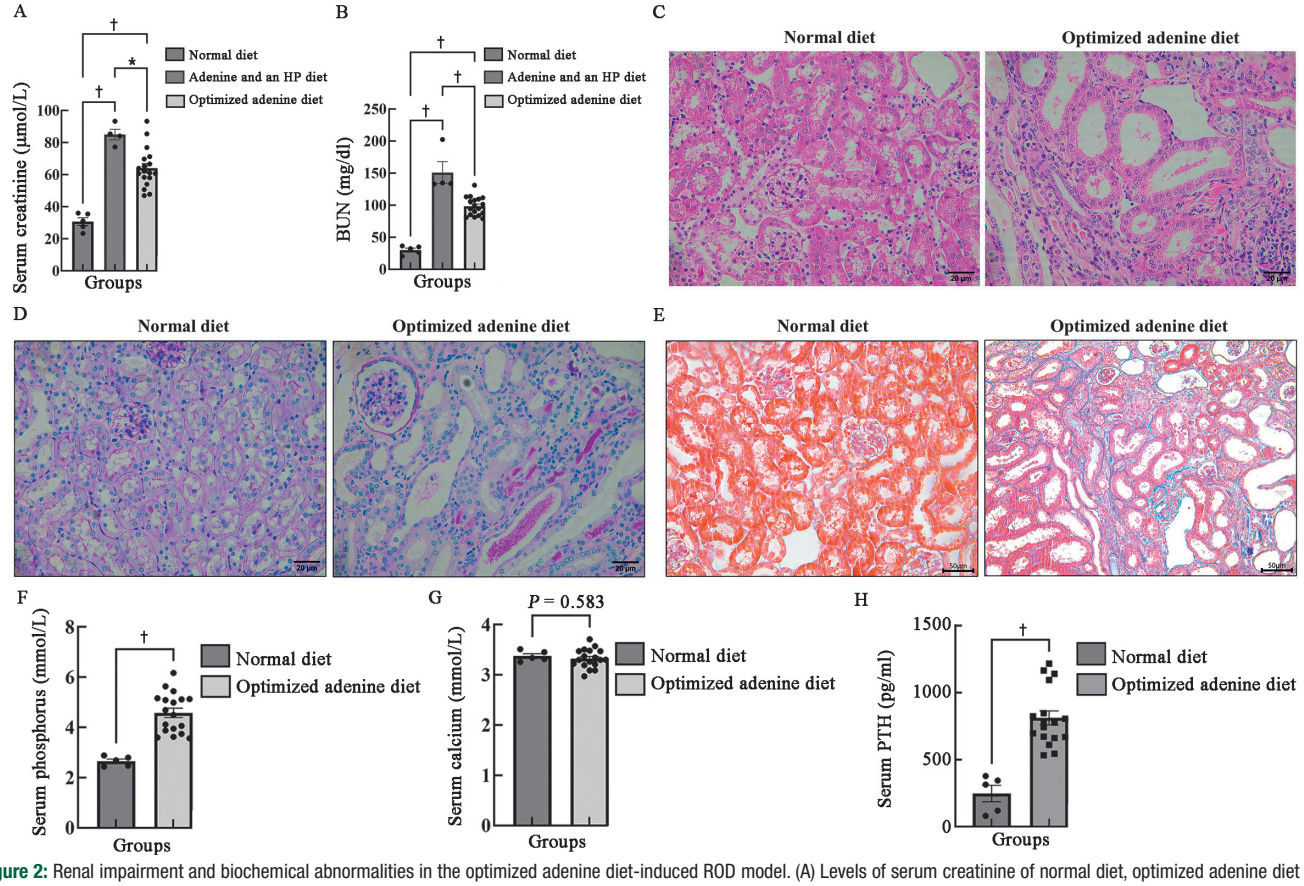

Figure 2: Renal impairment and biochemical abnormalities in the optimized adenine diet-induced ROD model. (A) Levels of serum creatinine of normal diet, optimized adenine diet and adenine and an HP diet (n = 5 for normal diet group, n = 4 for adenine and an HP diet, n = 20 for optimized adenine diet). (B) Levels of BUN in serum of normal diet, optimized adenine diet and adenine and an HP diet (n = 5 for normal diet group, n = 4 for adenine and an HP diet, n = 20 for optimized adenine diet). (C) Representative images of HE staining; Scale bar = 20 μm. (D) Representative images of PAS staining; Scale bar = 20 μm. (E) Representative images of Masson staining; Scale bar = 50 μm. (F) Levels of serum phosphorus (n = 5 for normal diet group, n = 18 for optimized adenine diet). (G) Levels of serum calcium (n = 5 for normal diet group, n = 18 for optimized adenine diet). (H) Levels of PTH (n = 5 for normal diet group, n = 17 for optimized adenine diet). Data are presented as mean ± SEM; Significant differences compared to the control group are indicated by $^{*}P$ <0.01 and $^{\dagger}P$ <0.001 vs. the control group. BUN: Blood urea nitrogen; HP: High-phosphate; PAS: Periodic acid-Schiff; PTH: Parathyroid hormone; ROD: Renal osteodystrophy; SEM: Standard error of the mean.

indicate that optimized adenine diet model mice have disrupted mineral metabolism.

Destruction of femur structure and bone turnover in model mice with optimized adenine diet-induced ROD

Micro-CT reconstructions revealed substantial structure destruction of the distal femur in the optimized adenine diet group [Figure 3A]. An adenine diet adversely affected the cortical bone at the femoral midshaft, with micro-CT reconstructions revealing severe cortical porosity. The trabecular bone parameters of the femur, which were measured using micro-CT, are presented in Figure 3B–F. BMD (Figure 3B, unpaired *t*-test with Welch's correction, $t = 5.12$, $P = 0.006$) at the distal femur was significantly lower in the model group than in the control group. This pattern was mirrored in the BV/TV (Figure 3C, unpaired *t*-test with Welch's correction, $t = 6.84$, $P < 0.001$), indicating similar deterioration. An assessment of trabecular parameters revealed a marked decrease in both Tb.N (Figure 3D, unpaired *t*-test with Welch's correction, $t = 3.47$, $P = 0.024$) and thickness (Tb.Th) (Figure 3E, unpaired *t*-test, $t = 4.76$, $P < 0.001$) in the model group, whereas Tb.Sp (Figure 3F, unpaired *t*-test, $t = 9.51$, $P < 0.001$) was significantly greater in the model group than in the control group. These results collectively suggest that the femoral structure of mice in the model group underwent severe degeneration.

TRAP staining facilitated the visualization of osteoclasts, which appeared pink, revealing an increase in osteoclasts in the model group [Figure 3G, H] (unpaired *t*-test with Welch's correction, $t = 3.01$, $P < 0.001$). Accordingly, the expression of osterix and cathepsin K in femur tissues were determined to assess the bone turnover status in model mice. Twelve weeks post-model induction, both osterix [Figure 3I, unpaired *t*-test with Welch's correction, $t = 7.56$, $P = 0.001$] and cathepsin K [Figure 3J, unpaired *t*-test with Welch's correction, $t = 4.63$, $P = 0.008$] levels were significantly elevated in the model group compared with those in the control group. These findings imply that model mice experienced substantial high-turnover bone pathology. In summary, the aforementioned results

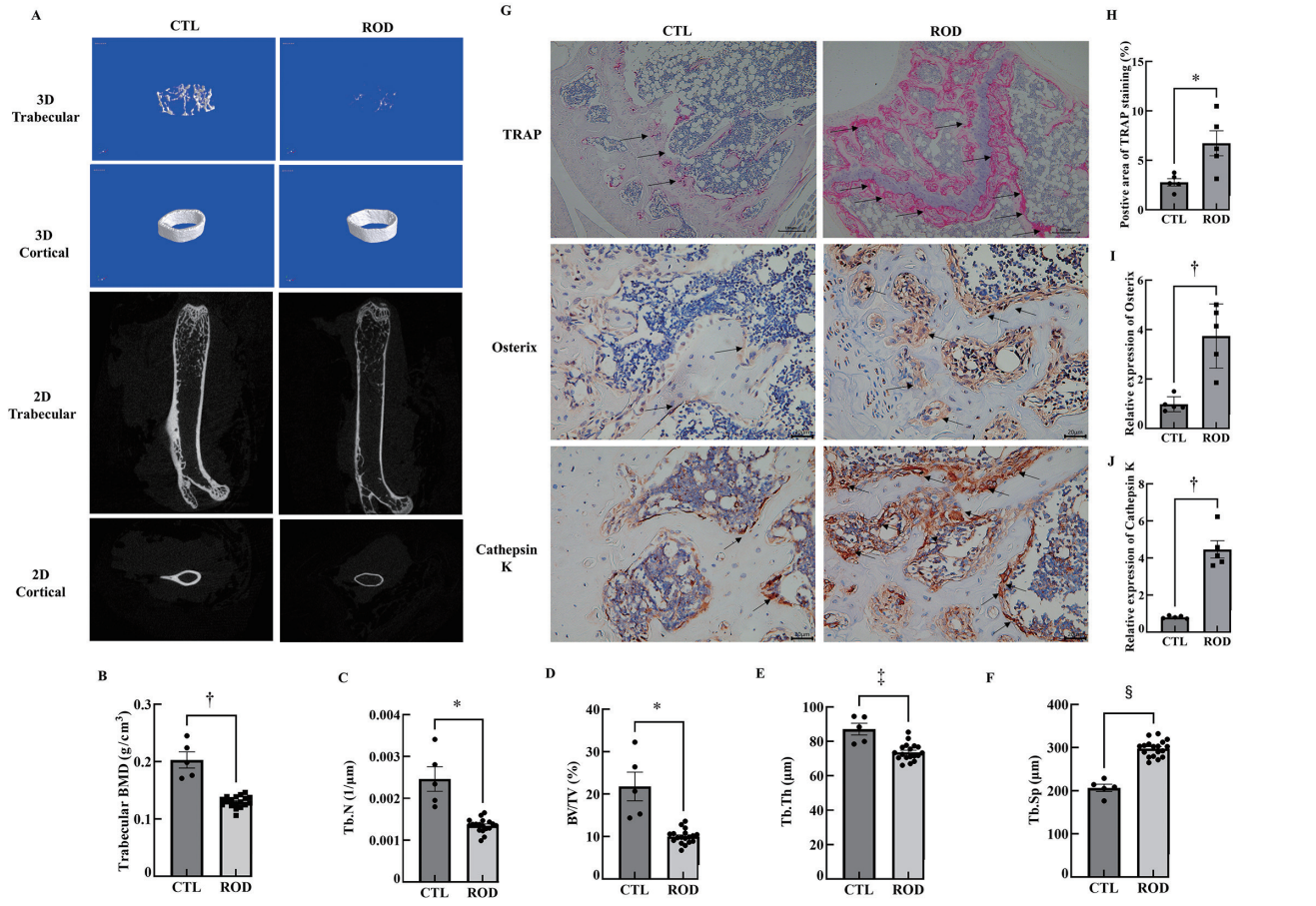

Figure 3: Histomorphometry and histopathological analysis of femurs in different groups. (A) Representative micro-CT reconstruction images of femurs from the two groups. (B) Trabecular BMD measured by micro-CT bone histomorphometry analysis ($n = 5$ for CTL group, $n = 18$ for ROD group). (C) Tb.N of different groups ($n = 5$ for CTL group, $n = 18$ for ROD group). (D) BV/TV of different groups ($n = 5$ for CTL group, $n = 18$ for ROD group). (E) Tb.Th of different groups ($n = 5$ for CTL group, $n = 18$ for ROD group). (F) Tb.Sp of different groups ($n = 5$ for CTL group, $n = 18$ for ROD group). (G) Upper: representative images of TRAP staining. Scale bar = 100 μm; Arrows indicate positively stained osteoclasts. Middle: IHC staining of osterix in the femur; scale bar = 20 μm. Arrows indicate regions of positive staining. Bottom: IHC staining of cathepsin K in the femur; scale bar = 20 μm. Arrows indicate regions of positive staining. (H) Positive area of TRAP staining ($n = 5$ per group). (I) Positive area of IHC staining of osterix ($n = 5$ per group). (J) Positive area of IHC staining of cathepsin K ($n = 5$ per group). Data are presented as mean ± SEM. $^{*}P < 0.05$, $^{\dagger}P < 0.01$, $^{\ddagger}P < 0.001$, and $^{\S}P < 0.0001$ *vs.* the control group. micro-CT: Microcomputed tomography; CTL: Control; ROD: Renal osteodystrophy; SEM: Standard error of the mean; BMD: bone mineral density. Tb.N: Trabecular number; BV: Bone volume; TV: Tissue volume; Tb.Th: Trabecular thickness; Tb.Sp: Trabecular separation; TRAP: Tartrate-resistant acid phosphatase; IHC: Immunohistochemistry.

substantiate the successful establishment of a stable and reliable murine ROD model that was characterized by impaired renal function, disturbances in mineral metabolism, and bone degeneration.

Identification and enrichment analysis of DEGs

Subsequent RNA-seq analysis of the right hind limbs (femurs and tibias) of the mice was conducted to elucidate the mechanisms underlying ROD. PCA was employed to confirm the repeatability of the data within each group, and the results revealed distinct distribution patterns between the ROD and CTL groups based on gene expression profiles. Within-group sample distances were notably compact along the first principal component (PC1) axis for both groups, as illustrated in Figure 4A, indicating clear group differentiation and excellent intragroup consistency. The expression profiles of 2630 genes with

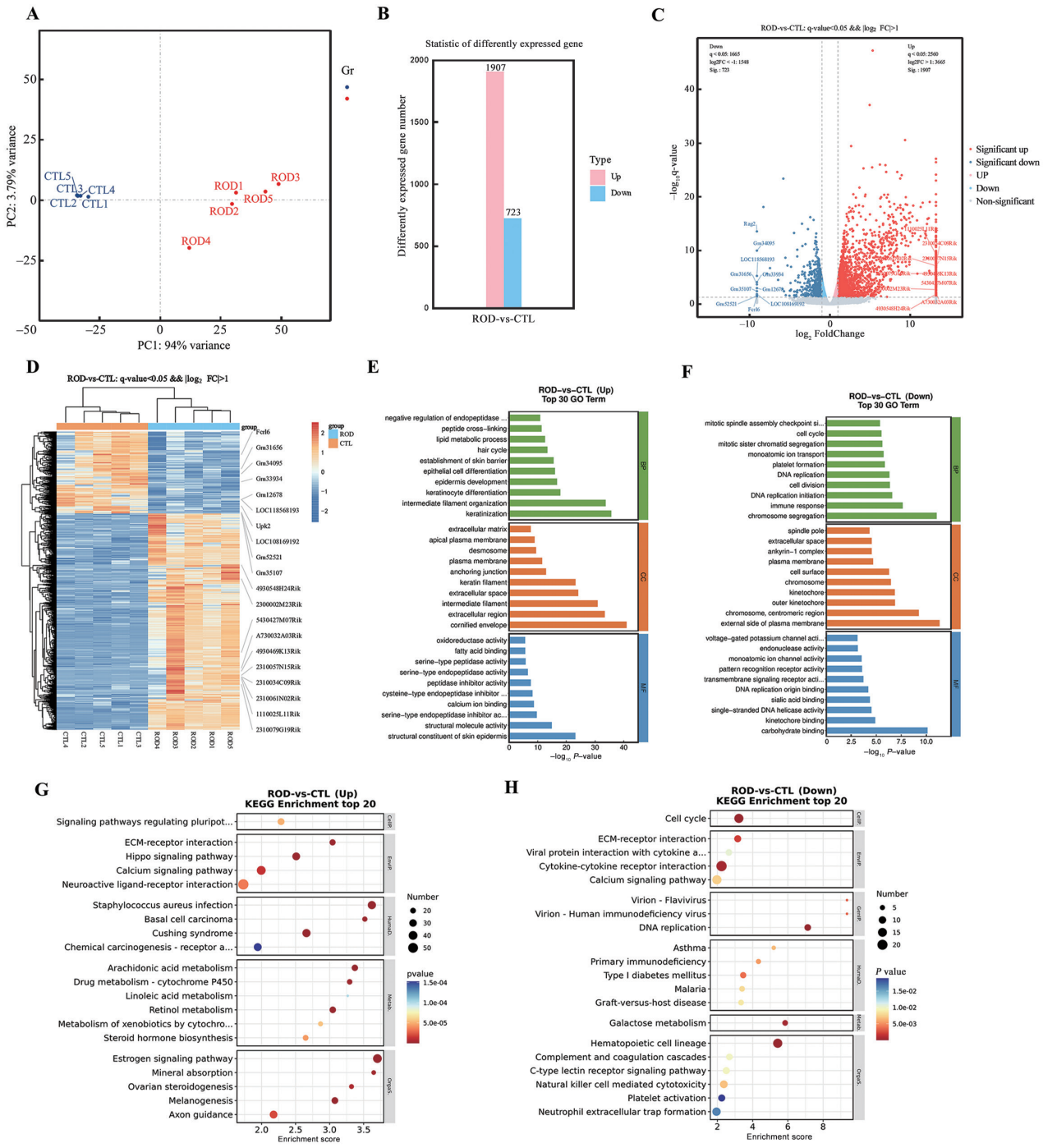

Figure 4: DEGs between ROD and CTL samples and functional enrichment. (A) PCA plot of samples after removing batch effect. (B) DEG numbers. (C) Volcano plot for DEGs. (D) Heat map for DEGs. (E) Top 30 upregulated GO pathways ranked by $-\log_{10}$ *P*-value. (F) Top 30 downregulated GO pathways ranked by $-\log_{10}$ *P*-value. (G) Top 20 significant upregulated KEGG pathways. (H) Top 20 significant downregulated KEGG pathways. CTL: Control; DEGs: Differentially expressed genes; GO: Gene ontology; KEGG: Kyoto Encyclopedia of Genes and Genomes; PC1: The first principal component; PC2: The second principal component; PCA: Principal component analysis; ROD: Renal osteodystrophy.

a significance threshold of $P < 0.05$ and a fold change of 2 or greater were identified. Among these DEGs, 1907 had upregulated expression, and 723 had downregulated expression [Figure 4B]. The distribution of these differing transcripts was visually depicted using a volcano plot [Figure 4C], and their relative expression levels are illustrated in the heatmap [Figure 4D]. GO enrichment analysis was performed to assess the potential functions and mechanisms of the DEGs within the domains of biological processes, cellular components, and molecular functions. The top 30 GO pathways with enrichment of DEGs with upregulated expression, ordered by *q*-value, are depicted in Figure 4E, while the top 30 pathways with enrichment of DEGs with downregulated expression are illustrated in Figure 4F. For the DEGs with upregulated expression, the three most enriched biological process terms were negative regulation of peptidase activity, peptide cross-linking, and lipid metabolic process. In contrast, the DEGs with downregulated expression were most significantly associated with mitotic spindle assembly checkpoint, cell cycle, and mitotic sister chromatid segregation. In terms of cellular components, the most significant terms were extracellular matrix for DEGs with upregulated expression and spindle pole for DEGs with downregulated expression. Molecular function analysis revealed that oxidoreductase activity was the most significantly enriched term for the DEGs with upregulated expression and voltage-gated potassium channel was that for the DEGs with downregulated expression. The top 20 KEGG pathways with significant enrichment of upregulated DEGs are presented in Figure 4G. In addition to the classical bone metabolism pathways, such as the calcium signaling pathway, notable enrichment was also observed in the Hippo signaling pathway and the estrogen signaling pathway. The top 20 KEGG pathways with significant enrichment of downregulated DEGs are delineated in Figure 4H. Among these pathways, pathways related to the cell cycle and cytokine–cytokine receptor interactions were significantly enriched.

GSEA and qRT-PCR validation of the upregulated expression of genes in the sphingolipid metabolism pathway

We used GSEA to examine enriched GO and KEGG pathways in the hind limb datasets. This approach was used to identify pivotal pathways and the central genes associated with ROD. Significantly, the sphingolipid metabolism pathway was indicated to be highly relevant to the pathogenesis of ROD. Visualizations of these enrichment analyses, including snapshots and a heatmap, are provided in Figure 5A, B.

Transcriptomic analysis of DEGs revealed involvement of the sphingolipid metabolism pathway, with upregulated genes including alkaline ceramidase 1 (*Acer1*), alkaline ceramidase 2 (*Acer2*), adenosine A1 receptor (*Adora1*), ceramide synthase 3 (*Cers3*), ceramide synthase 4 (*Cers4*), kininogen 2 (*Kng2*), sphingomyelin phosphodiesterase 3 (*Smpd3*), prosaposin-like 1 (*Psapl1*), sphingosine-1-phosphate receptor 5 (*S1pr5*), and sphingosine-1-phosphate phosphatase 2 (*Sgpp2*). Subsequent comparative quantitative RT-PCR analysis confirmed that all 10 genes were upregulated in the femur samples of ROD mice compared with those of the control (CTL) group. Notably, five of these genes (*Acer1, Acer2, Psapl1, Adora1*, and *S1pr5*) showed significant upregulation (Figure 5C, unpaired *t*-test, $t = 3.08$, $P = 0.015$; Figure 5D, unpaired *t*-test with Welch's correction, $t = 3.12$, $P = 0.036$; Figure 5H, unpaired *t*-test with Welch's correction, $t = 3.82$, $P = 0.019$; Figure 5I, unpaired *t*-test with Welch's correction, $t = 4.38$, $P = 0.008$; Figure 5J, unpaired *t*-test, $t = 3.09$, $P = 0.015$). The remaining five genes (*Cers3*, *Cers4*, *Sgpp2*, *Kng2*, *Smpd3*) showed no significant differences between the two groups [Figure 5].

Discussion

ROD is a multifaceted bone metabolism disorder that affects nearly all CKD patients, causing severe clinical complications such as bone loss, abnormal mineralization, fracture, and mortality. Current clinical approaches for treating ROD are ineffective and mainly involve addressing mineral imbalances such as imbalances in calcium, phosphate, vitamin D, and PTH levels due to a limited understanding of the underlying pathogenic mechanisms. A significant barrier in research on ROD pathogenesis is the absence of a stable and reliable animal model. Previous ROD animal models have not perfectly replicated the actual disease outcomes observed in humans. In our study, we developed a novel mouse model for ROD by adjusting the mineral concentrations to 1% phosphorus, 1% calcium, and 1 IU/g vitamin D, based on a purified feed containing 0.2% adenine, 19% protein, and 17% fat. Unlike previous adenine diet models based on general feed,[42] which is not public, the formulation of our optimized adenine diet model based on purified feed is transparent [Supplementary Material 2, http://links.lww.com/CM9/C115], thereby enhancing the reproducibility of results. Interestingly, our model mice had an increased mouse survival rate and improved renal function compared with the previous adenine and HP diet model mice. This phenomenon suggests that the strategic addition of phosphorus, calcium, and vitamin D to the diet may mitigate tubular injury, leading to these observed differences and enhancing the capacity of the mice to withstand prolonged induction periods. Unlike surgical ROD models, our model avoids variability and technical complexity, thereby increasing the feasibility, stability, and reliability of the model. Additionally, our ROD model more closely resembles the bone pathology observed in CKD patients than other models. Micro-CT and bone histopathological analysis revealed that the bone changes in our model mirror those observed in ROD patients, which are characterized by the bone structure destruction, bone loss, and high bone turnover. Bone biopsy is the gold standard for diagnosing renal osteodystrophy; however, its invasive nature poses significant challenges for routine clinical practice.[43] In addition, bone destruction is not commonly observed in the early stage of CKD-MBD and progresses in the later stages of CKD-MBD.[44] Hence, our model paves the way for future basic and clinical research on the pathogenesis of ROD.

The molecular mechanisms that contribute to bone pathologies in ROD are complex and not entirely understood.[45]

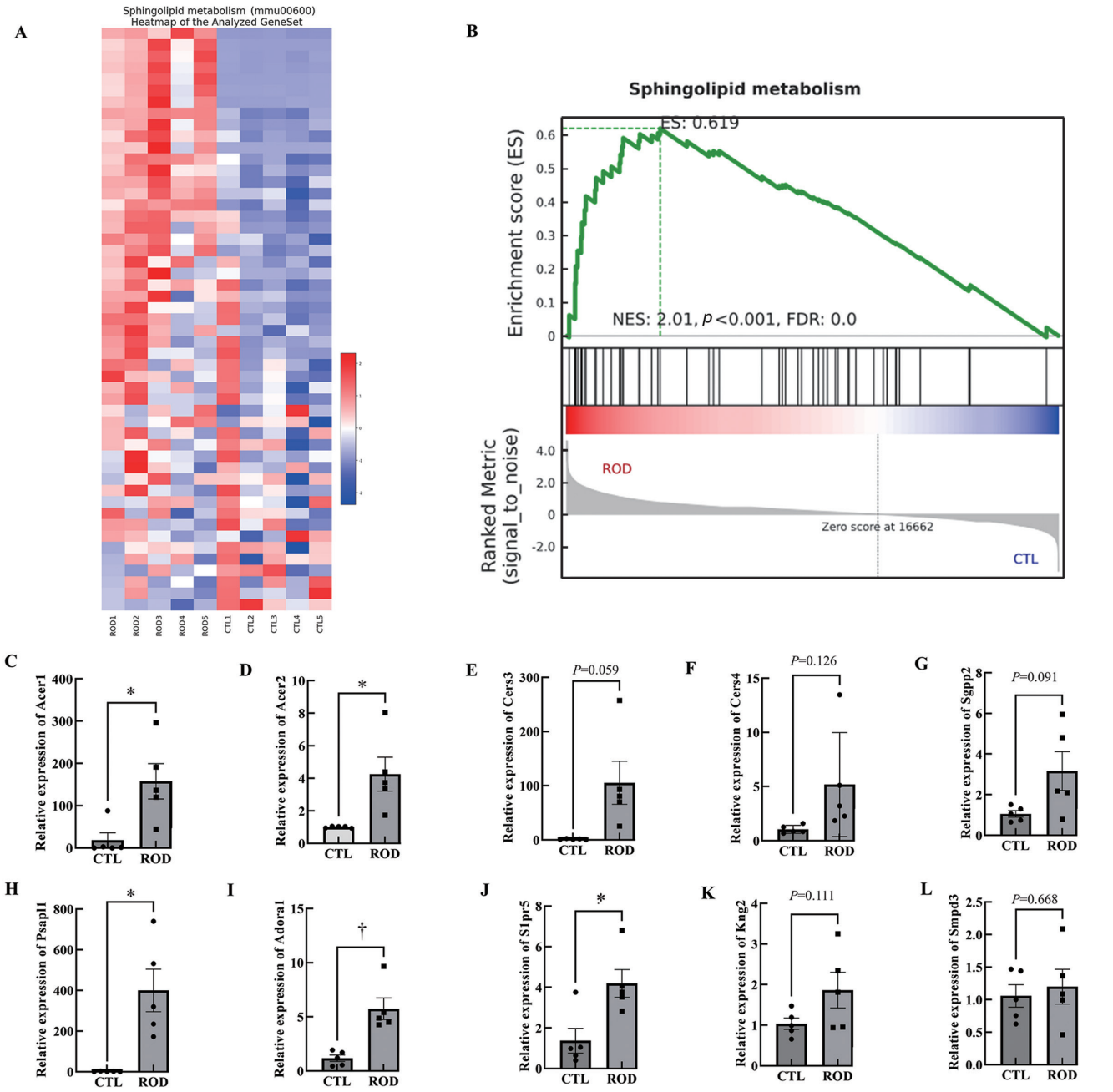

Figure 5: GSEA and qRT-PCR validation of the sphingolipid metabolism pathway. (A) Heat map for GSEA pathway analysis of the sphingolipid metabolism pathway. (B) GSEA snapshots of KEGG pathway enrichment analysis: sphingolipid metabolism pathway. Relative mRNA expression of (C) *Acer1*; (D) *Acer2*; (E); *Cers3*; (F) *Cers4*; (G) *Sgpp2*; (H) *Psapl1*; (I); *Adora1*; (J) *S1pr5*; (K) *Kng2*; and (L) *Smpd3* between the CTL group and ROD group ($n = 5$ per group). Data are presented as the mean ± SEM. $^{*}P < 0.05$, $^{\dagger}P < 0.01$. CTL: Control; GSEA: Gene set enrichment analysis; KEGG: Kyoto Encyclopedia of Genes and Genomes; qRT-PCR: Quantitative real-time polymerase chain reaction; ROD: Renal osteodystrophy; SEM: Standard error of the mean.

Recent advancements in next-generation sequencing (NGS) have enabled investigators to identify critical genes and pathways implicated in bone metabolism. RNA-seq is particularly informative for examining bone disorders and providing an exhaustive view of the biological landscape. To our knowledge, this is an pioneering study to explore the transcriptional molecular changes in the skeletal tissue of ROD mice via RNA-seq. Using RNA-seq, we identified the lipid metabolism process, especially the sphingolipid metabolism pathway, which is crucial for the pathogenesis of ROD. The differential expressed genes encoding key enzymes and receptors within this pathway, such as *Acer1*, *Acer2*, *Psapl1*, *Adora1*, and *S1pr5* were validated via qRT-PCR. Consequently, these genes are potential targets in ROD progression and need to be further investigated.

Our previous study showed that lipid metabolism plays a critical role in the pathogenesis of ROD.[46] More recently, studies have elucidated that sphingolipid metabolism plays a critical role on bone remodeling.[47,48] However, the role of sphingolipids in ROD has not been investigated. Our study provides new insights into ROD and highlights new potential therapeutic targets that could be

used to treat this complex bone disease in patients with CKD.

However, our study has several limitations. Although RNA-seq offers significant insights, it is unable to pinpoint specific gene expression variations in individual cells. Single-cell analysis (scRNA-seq), on the other hand, provides a detailed view of the transcriptional activities within individual cells. Nonetheless, scRNA-seq captures only approximately 10–20% of transcripts per cell.[49] Future studies could significantly deepen our understanding by merging RNA-seq and scRNA-seq techniques. Such an integrated approach would enable the precise identification of pathways within distinct cell populations, thereby bridging the gap in fundamental research into the pathophysiological mechanisms underlying ROD.

In summary, a novel mouse model for ROD was successfully developed by utilizing a modified adenine diet. This model exhibits severe skeletal abnormalities, analogous to those observed in patients with CKD-MBD, and thus represents a potentially valuable tool for further investigation of bone disease pathogenesis within this clinical context. Leveraging RNA-seq, we identified the sphingolipid metabolism pathway as a critical component in the development of ROD. This finding not only enhances our understanding of the disease mechanism but also unveils novel therapeutic targets for future investigations.

Acknowledgments

Gratitude is extended to the Kidney Disease Research Institute of Southeast University for providing the research platform. Thanks to Professor Jin Hui from the Department of Statistics, School of Public Health, Southeast University, for the assistance with the statistical methods of this paper.

Funding

This study was funded by the National Natural Science Foundation of China (No. 82370742) and the Key Program of Jiangsu Health and Health Committee (No. ZD2022045).

Conflicts of interest

None.

References

1. Ketteler M, Block GA, Evenepoel P, Fukagawa M, Herzog CA, McCann L, *et al*. Executive summary of the 2017 KDIGO chronic kidney disease-mineral and bone disorder (CKD-MBD) guideline update: What's changed and why it matters. Kidney Int 2017;92:26–36. doi: 10.1016/j.kint.2017.04.006.
2. Pazianas M, Miller PD. Osteoporosis and chronic kidney disease-mineral and bone disorder (CKD-MBD): Back to basics. Am J Kidney Dis 2021;78:582–589. doi: 10.1053/j.ajkd.2020.12.024.
3. Metzger CE, Swallow EA, Stacy AJ, Allen MR. Adenine-induced chronic kidney disease induces a similar skeletal phenotype in male and female C57BL/6 mice with more severe deficits in cortical bone properties of male mice. PLoS One 2021;23:e0250438. doi: 10.1371/journal.pone.0250438.
4. Metzger CE, Swallow EA, Allen MR. Elevations in cortical porosity occur prior to significant rise in serum parathyroid hormone in young female mice with adenine-induced CKD. Calcif Tissue Int 2020;06:392–400. doi: 10.1007/s00223-019-00642-w.
5. Chiu HW, Hou YC, Lu CL, Lu KC, Liu WC, Shyu JF, *et al*. Cinacalcet improves bone parameters through regulation of osteoclast endoplasmic reticulum stress, autophagy, and apoptotic pathways in chronic kidney disease-mineral and bone disorder. J Bone Miner Res 2022;37:215–225. doi: 10.1002/jbmr.4459.
6. Tani T, Orimo H, Shimizu A, Tsuruoka S. Development of a novel chronic kidney disease mouse model to evaluate the progression of hyperphosphatemia and associated mineral bone disease. Sci Rep 2017;22:2233. doi: 10.1038/s41598-017-02351-6.
7. Tatsumoto N, Arioka M, Yamada S, Takahashi-Yanaga F, Tokumoto M, Tsuruya K, *et al*. Inhibition of GSK-3β increases trabecular bone volume but not cortical bone volume in adenine-induced uremic mice with severe hyperparathyroidism. Physiol Rep 2016;4:e13010. doi: 10.14814/phy2.13010.
8. Lin W, Li Y, Chen F, Yin S, Liu Z, Cao W. Klotho preservation via histone deacetylase inhibition attenuates chronic kidney disease-associated bone injury in mice. Sci Rep 2017;7:46195. doi: 10.1038/srep46195.
9. Zhang Q, Liu L, Lin W, Yin S, Duan A, Liu Z, *et al*. Rhein reverses Klotho repression via promoter demethylation and protects against kidney and bone injuries in mice with chronic kidney disease. Kidney Int 2017;91:144–156. doi: 10.1016/j.kint.2016.07.040.
10. Gardinier JD, Daly-Seiler CS, Zhang C. Osteocytes' expression of the PTH/PTHrP receptor has differing effects on endocortical and periosteal bone formation during adenine-induced CKD. Bone 2020;133:115186. doi: 10.1016/j.bone.2019.115186.
11. Hsu SN, Stephen LA, Dillon S, Milne E, Javaheri B, Pitsillides AA, *et al*. Increased PHOSPHO1 expression mediates cortical bone mineral density in renal osteodystrophy. J Endocrinol 2022;254:153–167. doi: 10.1530/JOE-22-0097.
12. Ni LH, Tang RN, Lv LL, Wu M, Wang B, Wang FM, *et al*. A rat model of SHPT with bone abnormalities in CKD induced by adenine and a high phosphate diet. Biochem Biophys Res Commun 2018;498:654–659. doi: 10.1016/j.bbrc.2018.03.038.
13. Neven E, Vervaet B, Brand K, Gottwald-Hostalek U, Opdebeeck B, De Maré A, *et al*. Metformin prevents the development of severe chronic kidney disease and its associated mineral and bone disorder. Kidney Int 2018;94:102–113. doi: 10.1016/j.kint.2018.01.027.
14. Aoki C, Uto K, Honda K, Kato Y, Oda H. Advanced glycation end products suppress lysyl oxidase and induce bone collagen degradation in a rat model of renal osteodystrophy. Lab Invest 2013;93:1170–1183. doi: 10.1038/labinvest.2013.105.
15. Liu S, Song W, Boulanger JH, Tang W, Sabbagh Y, Kelley B, *et al*. Role of TGF-β in a mouse model of high turnover renal osteodystrophy. J Bone Miner Res 2014;29:1141–1157. doi: 10.1002/jbmr.2120.
16. Yaguchi A, Tatemichi S, Takeda H, Kobayashi M. PA21, a novel phosphate binder, improves renal osteodystrophy in rats with chronic renal failure. PLoS One 2017;12:e0180430. doi: 10.1371/journal.pone.0180430.
17. Davies MR, Lund RJ, Mathew S, Hruska KA. Low turnover osteodystrophy and vascular calcification are amenable to skeletal anabolism in an animal model of chronic kidney disease and the metabolic syndrome. J Am Soc Nephrol 2005;16:917–928. doi: 10.1681/ASN.2004100835.
18. Cejka D, Parada-Rodriguez D, Pichler S, Marculescu R, Kramer I, Kneissel M, *et al*. Only minor differences in renal osteodystrophy features between wild-type and sclerostin knockout mice with chronic kidney disease. Kidney Int 2016;90:828–834. doi: 10.1016/j.kint.2016.06.019.
19. González EA, Lund RJ, Martin KJ, McCartney JE, Tondravi MM, Sampath TK, *et al*. Treatment of a murine model of high-turnover renal osteodystrophy by exogenous BMP-7. Kidney Int 2002;61:1322–1331. doi: 10.1046/j.1523-1755.2002.00258.x.
20. Liu BH, Chong FL, Yuan CC, Liu YL, Yang HM, Wang WW, *et al*. Fucoidan ameliorates renal injury-related calcium-phosphate metabolic disorder and bone abnormality in the CKD-MBD model rats by targeting FGF23-klotho signaling axis. Front Pharmacol 2021;28:586725. doi: 10.3389/fphar.2020.586725.
21. Zhang X, Li T, Wang L, Li Y, Ruan T, Guo X, *et al*. Relative comparison of chronic kidney disease-mineral and bone disorder rat models. Front Physiol 2023;3:1083725. doi: 10.3389/fphys.2023.1083725.
22. Pawlak D, Domaniewski T, Znorko B, Pawlak K. The use of LP533401 as a therapeutic option for renal osteodystrophy affects,

renal calcium handling, vitamin D metabolism, and bone health in uremic rats. Expert Opin Ther Targets 2019;23:353–364. doi: 10.1080/14728222.2019.1586883.
23. Zhang DD, Wu YF, Chen WX, Xu Y, Liu SY, Luo HH, *et al*. C-type natriuretic peptide attenuates renal osteodystrophy through inhibition of FGF-23/MAPK signaling. Exp Mol Med 2019;51:1–18. doi: 10.1038/s12276-019-0265-8.
24. Ng AH, Willett TL, Alman BA, Grynpas MD. Development, validation and characterization of a novel mouse model of Adynamic Bone Disease (ABD). Bone 2014;68:57–66. doi: 10.1016/j.bone.2014.07.037.
25. Dussold C, Gerber C, White S, Wang X, Qi L, Francis C, *et al*. DMP1 prevents osteocyte alterations, FGF23 elevation and left ventricular hypertrophy in mice with chronic kidney disease. Bone Res 2019;25:12. doi: 10.1038/s41413-019-0051-1.
26. Courbon G, Francis C, Gerber C, Neuburg S, Wang X, Lynch E, *et al*. Lipocalin 2 stimulates bone fibroblast growth factor 23 production in chronic kidney disease. Bone Res 2021;9:35. doi: 10.1038/s41413-021-00154-0.
27. Martinez-Calle M, Courbon G, Hunt-Tobey B, Francis C, Spindler J, Wang X, *et al*. Transcription factor HNF4α2 promotes osteogenesis and prevents bone abnormalities in mice with renal osteodystrophy. J Clin Invest 2023;133:e159928. doi: 10.1172/JCI159928.
28. Biruete A, Metzger CE, Chen NX, Swallow EA, Vrabec C, Clinkenbeard EL, *et al*. Effects of ferric citrate and intravenous iron sucrose on markers of mineral, bone, and iron homeostasis in a rat model of CKD-MBD. Nephrol Dial Transplant 2022;37:1857–1867. doi: 10.1093/ndt/gfac162.
29. McNerny EMB, Buening DT, Aref MW, Chen NX, Moe SM, Allen MR. Time course of rapid bone loss and cortical porosity formation observed by longitudinal μCT in a rat model of CKD. Bone 2019;125:16–24. doi: 10.1016/j.bone.2019.05.002.
30. Kim K, Anderson EM, Thome T, Lu G, Salyers ZR, Cort TA, *et al*. Skeletal myopathy in CKD: A comparison of adenine-induced nephropathy and 5/6 nephrectomy models in mice. Am J Physiol Renal Physiol 2021;321:106–119. doi: 10.1152/ajprenal.00117.2021.
31. Martin A, David V. Transcriptomics: A solution for renal osteodystrophy? Curr Osteoporos Rep 2020;18:254–261. doi: 10.1007/s11914-020-00583-6.
32. David V, Salusky IB, Malluche H, Nickolas TL. Renal osteodystrophy: Something old, something new, something needed. Curr Opin Nephrol Hypertens 2023;32:559–564. doi: 10.1097/MNH.0000000000000918.
33. Chen S, Zhou Y, Chen Y, Gu J. Fastp: An ultra-fast all-in-one FASTQ preprocessor. Bioinformatics 2018;34:884–890. doi: 10.1093/bioinformatics/bty560.
34. Kim D, Langmead B, Salzberg SL. HISAT: A fast spliced aligner with low memory requirements. Nat Methods 2015;12:357–360. doi: 10.1038/nmeth.3317.
35. Roberts A, Trapnell C, Donaghey J, Rinn JL, Pachter L. Improving RNA-Seq expression estimates by correcting for fragment bias. Genome Biol 2011;12:R22. doi: 10.1186/gb-2011-12-3-r22.
36. Anders S, Pyl PT, Huber W. HTSeq – A Python framework to work with high-throughput sequencing data. Bioinformatics 2015;31:166–169. doi: 10.1093/bioinformatics/btu638.
37. Love MI, Huber W, Anders S. Moderated estimation of fold change and dispersion for RNA-Seq data with DESeq2. Genome Biol 2014;15:550. doi: 10.1186/s13059-014-0550-8.
38. The Gene Ontology Consortium. The gene ontology resource: 20 years and still going strong. Nucleic Acids Res 2019;47:330–338. doi: 10.1093/nar/gky1055.
39. Kanehisa M, Araki M, Goto S, Hattori M, Hirakawa M, Itoh M, *et al*. KEGG for linking genomes to life and the environment. Nucleic Acids Res 2008;36:480–484. doi: 10.1093/nar/gkm882.
40. Subramanian A, Tamayo P, Mootha VK, Mukherjee S, Ebert BL, Gillette MA, *et al*. Gene set enrichment analysis: A knowledge-based approach for interpreting genome-wide expression profiles. Proc Natl Acad Sci U S A 2005;102:15545–15550. doi: 10.1073/pnas.0506580102.
41. Mootha VK, Lindgren CM, Eriksson KF, Subramanian A, Sihag S, Lehar J, *et al*. PGC-1alpha-responsive genes involved in oxidative phosphorylation are coordinately downregulated in human diabetes. Nat Genet 2003;34:267–273. doi: 10.1038/ng1180.
42. Zicarelli F, Sarubbi F, Iommelli P, Grossi M, Lotito D, Lombardi P, *et al*. Nutritional characterization of hay produced in Campania Region: Analysis by the near infrared spectroscopy (NIRS) technology. Animals (Basel) 2022;12:3035. doi: 10.3390/ani12213035.
43. Dalle Carbonare L, Valenti MT, Giannini S, Gallieni M, Stefani F, Ciresa R, *et al*. Bone biopsy for histomorphometry in chronic kidney disease (CKD): State-of-the-art and new perspectives. J Clin Med 2021;10:4617. doi: 10.3390/jcm10194617.
44. Jørgensen HS, Behets G, Viaene L, Bammens B, Claes K, Meijers B, *et al*. Diagnostic accuracy of noninvasive bone turnover markers in renal osteodystrophy. Am J Kidney Dis 2022;79:667–676. doi: 10.1053/j.ajkd.2021.07.027.
45. Moe S, Drüeke T, Cunningham J, Goodman W, Martin K, Olgaard K, *et al*. Kidney disease: Improving global outcomes (KDIGO). Definition, evaluation, and classification of renal osteodystrophy: A position statement from kidney disease: Improving global outcomes (KDIGO). Kidney Int 2006;69:1945–1953. doi: 10.1038/sj.ki.5000414.
46. Ni LH, Tang RN, Yuan C, Song KY, Wang LT, Zhang XL, *et al*. Cinacalcet attenuated bone loss via inhibiting parathyroid hormone-induced endothelial-to-adipocyte transition in chronic kidney disease rats. Ann Transl Med 2019;7:312. doi: 10.21037/atm.2019.06.44.
47. Wang B, Wang H, Li Y, Song L. Lipid metabolism within the bone micro-environment is closely associated with bone metabolism in physiological and pathophysiological stages. Lipids Health Dis 2022;21:5. doi: 10.1186/s12944-021-01615-5.
48. Qi T, Li L, Weidong T. The role of sphingolipid metabolism in bone remodeling. Front Cell Dev Biol 2021;9:752540. doi: 10.3389/fcell.2021.752540.
49. Ayturk UM, Jacobsen CM, Christodoulou DC, Gorham J, Seidman JG, Seidman CE, *et al*. An RNA-seq protocol to identify mRNA expression changes in mouse diaphyseal bone: applications in mice with bone property altering Lrp5 mutations. J Bone Miner Res 2013; 28:2081–2093. doi: 10.1002/jbmr.1946.

How to cite this article: Wang YJ, Di Y, Li YQ, Lu J, Ji BF, Zhang YX, Chen ZQ, Chen SJ, Liu BC, Tang RN. Role of sphingolipid metabolism signaling in a novel mouse model of renal osteodystrophy based on transcriptomic approach. Chin Med J 2024;XXX:1–11. doi: 10.1097/CM9.0000000000003261